JOURNAL OF CHEMICAL PHYSICS VOLUME 120, NUMBER 3 15 JANUARY 2004

Electron and nuclear dynamics of molecular clusters in ultraintense laser fields. II. Electron dynamics and outer ionization of the nanoplasma

Isidore Last and Joshua Jortner[a)]
School of Chemistry, Tel Aviv University, Ramat Aviv, 69978 Tel Aviv, Israel

(Received 22 November 2002; accepted 8 October 2003)

We explore electron dynamics in molecular $(CD_4)_{1061}$ clusters and elemental Xe_n ($n=249-2171$) clusters, responding to ultraintense (intensity $I=10^{16}-10^{19}\,\mathrm{W\,cm^{-2}}$) laser fields. Molecular dynamics simulations (including magnetic field and relativistic effects) and analyses of high-energy electron dynamics and nuclear ion dynamics in a cluster interacting with a Gaussian shaped laser field (frequency 0.35 fs^{-1}, photon energy 1.44 eV, phase 0, temporal width 25 fs) elucidated the time dependence of inner ionization, the formation of a nanoplasma of unbound electrons within the cluster or its vicinity, and of outer ionization. We determined the cluster size and the laser intensity dependence of these three sequential-parallel electronic processes. The characteristic times for cluster inner ionization (τ_{ii}) and for outer ionization (τ_{oi}) fall in the femtosecond time domain, i.e., $\tau_{ii}=2-9$ fs and $\tau_{oi}=4-15$ fs for $(CD_4)_{1061}$, $\tau_{ii}=7-30$ fs and $\tau_{oi}=5-13$ fs for Xe_n ($n=479,1061$), with both τ_{ii} and τ_{oi} decreasing with increasing I, in accord with the barrier suppression ionization mechanism for inner ionization of the constituents and the cluster barrier suppression ionization mechanism for outer ionization. The positive delay times $\Delta\tau_{OI}$ between outer and inner ionization (e.g., $\Delta\tau_{OI}=6.5$ fs for Xe_n at $I=10^{16}\,\mathrm{W\,cm^{-2}}$ and $\Delta\tau_{OI}=0.2$ fs for $(CD_4)_{1061}$ at $I=10^{19}\,\mathrm{W\,cm^{-2}}$) demonstrate that the outer/inner ionization processes are sequential. For $(CD_4)_{1061}$, $\tau_{ii}<\tau_{oi}$, as appropriate for sequential outer/inner ionization dynamics, while for Xe_n clusters $\tau_{ii}>\tau_{oi}$, reflecting on the energetic hierarchy in the ionization of the Xe atoms. Quasiresonance contributions to the outer ionization of the nanoplasma were established, as manifested in the temporal oscillations in the inner/outer ionization levels, and in the center of mass of the nanoplasma electrons. The formation characteristics, dynamics, and response of the nanoplasma in molecular or elemental clusters were addressed. The nanoplasma is positively charged, with a high-average electron density $[\rho_P=(2-3)10^{22}\,\mathrm{cm^{-3}}]$, being characterized by high-average electron energies ϵ_{av} (e.g., in Xe_{1061} clusters $\epsilon_{av}=54$ eV at $I=10^{16}\,\mathrm{W\,cm^{-2}}$ and $\epsilon_{av}=0.56-0.37$ keV at $I=10^{18}\,\mathrm{W\,cm^{-2}}$, with $\epsilon_{av}\propto I^{1/2}$). Beyond the cluster boundary the average electron energy markedly increases, reaching electron energies in the range of 1.2–40 keV for outer ionization of Xe_n ($n=249-2171$) clusters. The nanoplasma exhibits spatial inhomogeneity and angular anisotropy induced by the laser field. Femtosecond time scales are predicted for the nanoplasma production (rise times 7–3 fs), for the decay (decay times ~5 fs), and for the persistence time (30–10 fs) of a transient nanoplasma at $I=10^{17}-10^{18}\,\mathrm{W\,cm^{-2}}$. At lower intensities of $I=10^{16}\,\mathrm{W\,cm^{-2}}$ a persistent nanoplasma with a ''long'' lifetime of >50 fs will prevail. [DOI: 10.1063/1.1630308]

I. INTRODUCTION

Features of light-matter interactions emerge from experimental[1–9] and theoretical[10–20] studies of extreme multielectron ionization of molecular clusters, e.g., $(Xe)_n$, $(D_2)_n$, or $(CD_4)_n$ in ultraintense laser fields (peak intensity $I=10^{15}-10^{20}\,\mathrm{W\,cm^{-2}}$). The response of a large, finite molecular cluster to ultraintense laser fields is distinct from the response of ''small'' atoms and molecules.[21–23] While the ionization of single atomic and molecular systems in ultraintense laser fields is triggered by the barrier suppression ionization (BSI) single-step mechanism,[24,25] the electron dynamics of clusters in ultraintense laser fields involves three sequential-parallel processes: (1) inner ionization,[10,12,13,16,25] which involves the stripping of the cluster atoms of their valence electrons or of all their electrons, with the inner ionization level being mainly determined by the electronic structure of the atoms and by the laser intensity; (2) the formation of an energetic electron-positive ion charged nanoplasma within the cluster (and in its vicinity), which consists of unbound electrons interacting with the ultraintense laser field;[10,13,16,25] and (3) outer ionization,[10–20,25] which removes all or part of the unbound electrons of the charged nanoplasma from the cluster. These three electronic processes in ultraintense laser fields are coupled to each other. Subsequent and parallel to outer ionization, the electronic dynamic processes trigger nuclear dynamics, with the outer ionization being accompanied by cluster Coulomb explosion,[10,12–18] which results in the production of energetic (keV–MeV) multicharged ions. Generally speaking, the electronic dynamic processes and the nuclear process of Coulomb explosion are hierarchical.

The unique features of ultraintense laser-molecular clus-

a)Electronic mail: jortner@chemsgl.tau.ac.il

0021-9606/2004/120(3)/1348/13/$22.00

ter interactions involve mechanisms of extreme multielectron ionization and characteristics of electron dynamics. In an accompanying paper[25] (referred to as Paper I), we studied extreme cluster multielectron ionization involving the removal of the valence electrons or the complete stripping of all the electrons from the cluster constituents, with the formation of bare nuclei from light first-row atoms, or the formation of highly charged heavy ions, e.g., Xe^{q+} ($q \leqslant 36$) from heavy atoms. In this article, we explore features of electron dynamics in molecular $(CD_4)_n$ and elemental Xe_n ($n=55$–1061) clusters, responding to ultraintense ($I = 10^{16}$–10^{19} W cm^{-2}) laser fields. The following issues arise in the context of molecular cluster electron dynamics in ultraintense laser fields:

(1) What are the time scales for the three distinct sequential-parallel electronic processes, involving inner ionization, the formation of a nanoplasma of unbound electrons, and outer ionization, and how are they affected by the laser intensity and by the size of the molecular cluster?

(2) How is the electron dynamics for the three distinct fundamental electronic processes affected by the temporal shape of the laser pulse? Inner ionization, nanoplasma formation and response, and outer ionization involve laser driven processes, for which one cannot separate the electron dynamics from the time evolution of the laser pulse, which is coupled to the nuclear-electronic system.

(3) What are the characteristics of formation, properties, and dynamics of the electron-positive ion charged nanoplasma in molecular clusters in ultraintense laser fields?

Our simulations and analyses will shed light on the new facets of electron dynamics.

II. TIME-RESOLVED INNER AND OUTER IONIZATION PROCESSES

A. Methodology

The methodology of the simulations of the high-energy electron dynamics and of nuclear (ion) dynamics were reported in Paper I. Briefly, the laser electric field F_ℓ was taken as

$$F_\ell = F_{\ell 0}(t)\cos(2\pi\nu t + \varphi_0) \quad (1)$$

being characterized by a Gaussian shaped envelope function of the pulse

$$F_{\ell 0}(t) = F_M \exp[-2.773(t/\tau)^2] \quad (2)$$

with the parameters of frequency $\nu = 0.35$ fs^{-1} (photon energy of 1.44 eV), phase $\varphi_0 = 0$, and temporal width $\tau = 25$ fs [full width at half maximum of the intensity profile of 18 fs]. The electric field maximum F_M is related to the peak intensity I (in W cm^{-2}) by

$$|eF_M| = 2.745\times 10^{-7}(I^{1/2}) \quad \text{eV Å}^{-1}. \quad (3)$$

We note in passing that the laser field, Eqs. (1) and (2), is defined in the temporal range $t > -\infty$, and the peak of the laser pulse is attained at $t=0$. An initially truncated Gaussian pulse was used in the simulations, with the initial laser field $F_\ell = F_s$ being located at the finite (negative) time $t = t_s$, with the choice $F_s = (F^{th} + F^{co})/2$, where F^{th} is the threshold field

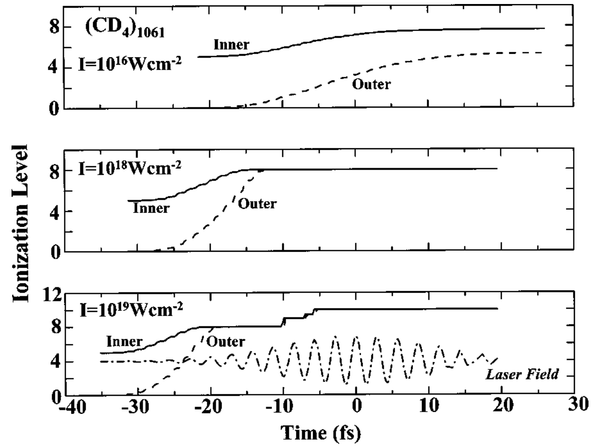

FIG. 1. Time-resolved electron dynamics of $(CD_4)_{1061}$ clusters driven by a Gaussian shaped laser field, Eqs. (1) and (2), which is represented in arbitrary units (with $F_\ell = 0$ at 4.0) by a dashed-dotted curve (—·—·—·—) in the lower panel. The time scales for $t \geqslant t_s$ (with $t_s < 0$ defined in the text) represent the time-dependent electron dynamics on the time scale of the laser pulse, which peaks at $t=0$. The time-dependent inner ionization level (——) and outer ionization level (— — —), which are defined by the number of electrons per CD_4 molecule, are marked on the curves. Upper panel: $I = 10^{16}$ W cm^{-2}; middle panel: $I = 10^{18}$ W cm^{-2}; and lower panel: $I = 10^{19}$ W cm^{-2}.

for the first (single electron) ionization of each molecule, while F^{co} is the laser field for complete one-electron ionization of all the constituent atoms within the molecular cluster [i.e., for $(CD_4)_n$ the complete one-electron ionization level per molecule is 5, while for Xe_n the complete ionization laser per atom is 1]. At the initial laser field F_s (Table II of Paper I) at $t = t_s$, all the cluster atoms are taken as singly charged ions, with the electrons initially located at $r = x_b$ from each ionic center, where x_b is the characteristic barrier suppression ionization (BSI) distance, Eq. (2a) of Paper I. The cluster inner ionization, which is driven by a composite field consisting of the laser field and the inner field, was described in terms of the BSI for each constituent. An additional, small ($\lesssim 13\%$), contribution to the inner ionization originates from electron impact ionization. The simulations of the molecular dynamics of the energetic electrons and of the ions were performed by classical molecular dynamics, incorporating electron–electron, electron–ion, ion–ion, and electron/ion-laser interactions. High-energy electron dynamics involved relativistic effects and were subjected to magnetic effects for electron-laser interactions. These simulation results provide a complete picture of electron-nuclear dynamics, including hydrodynamic effects.[2,26]

B. Time dependence of inner and outer ionization

Figures 1–3 display the simulation results for electron dynamics, as characterized by the time dependence of the inner and the outer ionization levels in $(CD_4)_{1061}$ and Xe_n ($n = 459$ and 1061) molecular clusters, as induced by a Gaussian laser field, Eqs. (1)–(3), where the temporal laser profile is also presented in these figures. The electron dynamics correspond to one complete laser temporal pulse profile. The ionization levels are given in Figs. 1, 2, and 3 in terms of electrons depleted per constituent atom (for Xe_n) or per

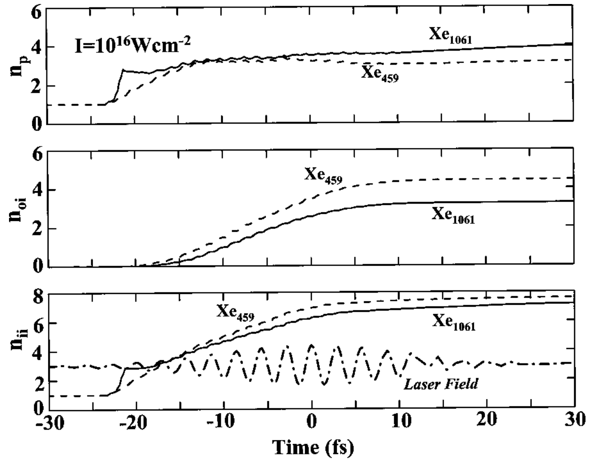

FIG. 2. Time-resolved electron dynamics in Xe_{1061} and Xe_{459} clusters driven by a Gaussian shaped laser field, Eqs. (1) and (2), which is represented in arbitrary units (with $F_\ell=0$ at 3.0) by a dashed-dotted (—·—·—) curve in the lower panel. The laser peak intensity is $I=10^{16}\,\mathrm{W\,cm^{-2}}$. The time scales for $t>t_s$ (with $t_s<0$ defined in the text) represent the time-dependent electron dynamics on the time scale of the laser pulse, which peaks at $t=0$. The time-dependent inner ionization levels (n_{ii}), outer ionization levels (n_{oi}), and the nanoplasma population (n_p) are defined in terms of the number of electrons per Xe atom in the cluster. The time-dependent data are given for the Xe_{1061} (——) and Xe_{459} (— — —) clusters, as marked on the curves. Lower panel: n_{ii} data; middle panel: n_{oi} data; and upper panel: n_p data.

molecule [for $(CD_4)_n$]. These are represented by the time-dependent inner ionization level n_{ii}, which corresponds to the number of electrons removed from each cluster constituent atom or molecule and the time-dependent outer ionization level n_{oi}, which represents the number of electrons per constituent removed from the cluster to infinity. (This is specified in Paper I by the electron removal to a distance of $>6R$. As the electron energies do not increase by more than 50% above this spatial limit, such a characterization of the outer ionization domain is appropriate.) The total number of electrons resulting from inner and from outer ionization of a cluster containing n constituents are nn_{ii} and nn_{oi}, respectively. The electron population n_p of the nanoplasma is characterized by the time-dependent number of electrons per constituent of $n_p(t)=n_{ii}(t)-n_{oi}(t)$ and a total number of electrons of nn_p.

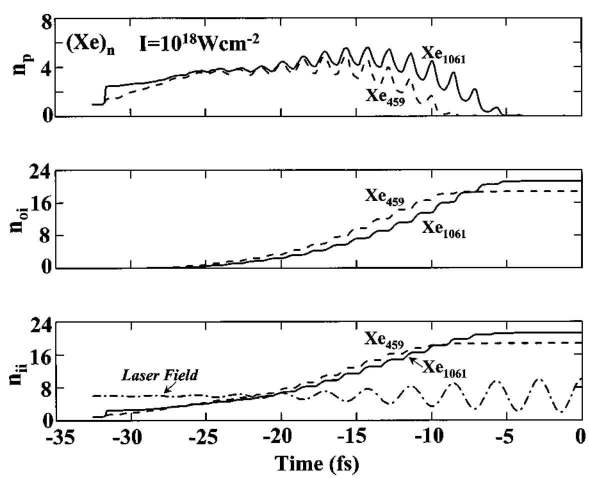

FIG. 3. Time-resolved electron dynamics in Xe_{1061} clusters (——) and in Xe_{459} clusters (— — —) driven by a Gaussian shaped laser field, Eqs. (1) and (2), which is represented in the lower panel in arbitrary units (with $F_\ell=0$ at 6.0) by a dashed-dotted (—·—·—) curve. The laser peak intensity is $I=10^{18}\,\mathrm{W\,cm^{-2}}$. The ionization levels are defined per Xe atom in the cluster. Notation and data representation as in Fig. 2.

In Table I we present the initial values $n_{ii}(t_s)$ for the inner ionization level, and $n_{oi}(t_s)$ for the outer ionization level at $t=t_s$ (defined by the initial conditions for n_{ii} and by $n_{oi}=0$). In Table I we also present the final values of the inner/outer ionization levels, which correspond to the long-time asymptotic values $(n_{ii})_{sat}$ and $(n_{oi})_{sat}$, respectively, as well as the asymptotic values $(n_p)_{sat}$ of the electron populations of the nanoplasma $(n_p)_{sat}=(n_{ii})_{sat}-(n_{oi})_{sat}$. For both $(CD_4)_{1061}$ and Xe_n clusters ($n=459,1061$) we note the occurrence of finite values of $(n_p)_{sat}$ at $I=10^{16}\,\mathrm{W\,cm^{-2}}$, while for higher intensities of $I=10^{18}$, $10^{19}\,\mathrm{W\,cm^{-2}}$, $(n_p)_{sat}=0$, marking a complete outer ionization of the nanoplasma.

C. Time-resolved impact ionization yields

The two mechanisms for cluster inner ionization involve the majority contribution of BSI of the constituents, which is induced by the composite laser+inner ionization field, and the minority contribution of impact ionization.[13,25] Both these contributions are included in the $n_{ii}(t)$ data of Figs. 1–3. The relative asymptotic value ratios for the impact ionization/BSI yields in $(CD_4)_n$ and Xe_n clusters manifest laser intensity dependence (decreasing with increasing I) and cluster size (R^2) dependence, being of the order of a few percent (Paper I). In Fig. 4 we present the time dependence of the total number of electrons, N_{imp}, produced by impact ionization in $(CD_4)_{1061}$ and Xe_{1061} molecular clusters. The contribution of impact ionization to the asymptotic ionization level $(n_{ii})_{sat}$ (per cluster constituent) is N_{imp}/n. For $(CD_4)_{1061}\,N_{imp}/n=1.0$ at $I=10^{16}\,\mathrm{W\,cm^{-2}}$, and $N_{imp}/n=0.46$ at $I=10^{18}\,\mathrm{W\,cm^{-2}}$, while for $Xe_{1061}\,N_{imp}/n=0.69$ at $I=10^{16}\,\mathrm{W\,cm^{-2}}$ and $N_{imp}/n=0.20$ at $I=10^{18}\,\mathrm{W\,cm^{-2}}$. From these asymptotic data we conclude that for a given molecular cluster, N_{imp}/n decreases with increasing the laser intensity, as already inferred from the simulations presented in Paper I for the total inner ionization yield. A cursory examination of the time-resolved impact ionization data (Fig. 4) reveals that the long time limit for the attainment of saturation of N_{imp}/n at $I=10^{16}\,\mathrm{W\,cm^{-2}}$ is manifested at longer times than the corresponding times for near saturation of inner ionization (characterized by inner saturation levels of 95%, as subsequently defined in Sec. II D). On the other hand, at $I=10^{18}\,\mathrm{W\,cm^{-2}}$ the saturation onset for impact ionization nearly coincides with t_{ii} (Fig. 4), however, at this high intensity the contribution of the impact ionization is small. Accordingly, at $I=10^{16}\,\mathrm{W\,cm^{-2}}$, a substantial contribution to the impact inner ionization level occurs sequentially to the BSI inner ionization. This impact ionization minority component provides a long-time tail for the time evolution of the inner ionization. We found that this long-time tail of electron dynamics is not important for the nuclear dynamics, i.e., time scales and ion energetics of cluster Coulomb explosion.

TABLE I. Electron dynamics in molecular clusters.[a]

Cluster	I W cm^{-2}	$n_{ii}(t_s)$[c]	$(n_{ii})_{sat}$[c]	$n_{oi}(t_s)$[c]	$(n_{oi})_{sat}$[c]	$(n_p)_{sat}$[c]	$\Delta\tau_{OI}$ fs[d]	τ_{ii} fs[e]	τ_{oi} fs[e]
$(CD_4)_{1061}$	10^{16}	5	7.7	0	5.1	2.6	3.8	8.9	15.2
	10^{18}	5	8	0	8	0	3.1	3.9	4.4
	10^{19}	5	8	0	8	0	2.2	2.8	3.9
	10^{19}[b]	8	10	8	10	0	0.2	4.0	4.2
Xe_{459}	10^{16}	1	7.7	0	4.3	3.2	6.4	18.5	13.4
	10^{18}	1	18.7	0	18.7	0	2.2	7.0	5.5
Xe_{1061}	10^{16}	1	7.3	0	3.2	4.1	6.5	29.1	12.8
	10^{18}	1	21.3	0	21.3	0	3.4	8.4	5.8

[a]Simulation data for a Gaussian laser field, Eqs. (1) and (2), with the initial laser field F_s (at $t=t_s$; $-\infty<t_s<0$) defined in Sec. II A.

[b]Two-step temporal multielectron ionization involving the inner (outer) ionization processes 5→8 (0→8) and 8→10 (8→10).

[c]Initial $n_{ii}(t_s)$ and final asymptotic $(n_{ii})_{sat}$ values for the numbers of electrons per constituent molecules or atoms for inner ionization (n_{ii}), for outer ionization (n_{oi}) and for the asymptotic value $n_p(\infty)$ of the nanoplasma electrons.

[d]The time lag $\Delta\tau_{OI}=t_{oi}^{(1/2)}-t_{ii}^{(1/2)}$ between half values of the rise times of electron populations for outer and inner ionization.

[e]Characteristic times for inner ionization (τ_{ii}) and for outer ionization (τ_{oi}), Eq. (6).

D. Time scales and yields for inner and outer ionization

The initial ionization levels for inner/outer ionization are specified in terms of the initial values of $n_{ii}(t_s)$ and $n_{oi}(t_s)=0$, discussed above. The times for the onset of inner and of outer ionization will be denoted by t_{ii}^{ons} and t_{oi}^{ons}, respectively. t_{ii}^{ons} corresponds to the initial rise of $[n_{ii}(t_{ii}^{ons})-n_{ii}(t_s)]/(n_{ii})_{sat}$ by 0.05, while t_{oi}^{ons} corresponds to the initial rise of $n_{oi}(t_{oi}^{ons})/(n_{oi})_{sat}$ by 0.05. The final ionization levels for inner/outer ionization are given by the long-time saturation values of $n_{ii}(t)$ and of $n_{oi}(t)$, being denoted as $(n_{ii})_{sat}$ and $(n_{oi})_{sat}$, respectively (Figs. 1–3 and Table I). The saturation times t_{ii} for inner ionization are defined for the attainment of 95% of the saturation value $(n_{ii})_{sat}$, i.e., $n_{ii}(t_{ii})/(n_{ii})_{sat}=0.95$ as discussed above. This choice of t_{ii} was motivated by disregarding the contribution of the long-time tail for impact ionization for $I=10^{16}$ W cm^{-2} (Fig. 4 and Sec. II C). Similarly, the saturation times t_{oi} for outer ionization were defined by $n_{oi}(t_{oi})/(n_{oi})_{sat}=0.95$. The values of the onset and saturation times t_{ii}^{ons}, t_{oi}^{ons}, t_{ii}, and t_{oi}, together with the corresponding ionization levels, are presented in Fig. 5. These onset and saturation times are given for the laser envelope Eqs. (1) and (2), used in our simulations.

For the $(CD_4)_{1061}$ cluster (Figs. 1 and 5 and Table I), the inner ionization levels at $I=10^{16}$ W cm^{-2} and at $I=10^{18}$ W cm^{-2} increase in a single gradual step from $n_{ii}=5$ (corresponding to the $C^+D_4^+$ molecule) and saturate at

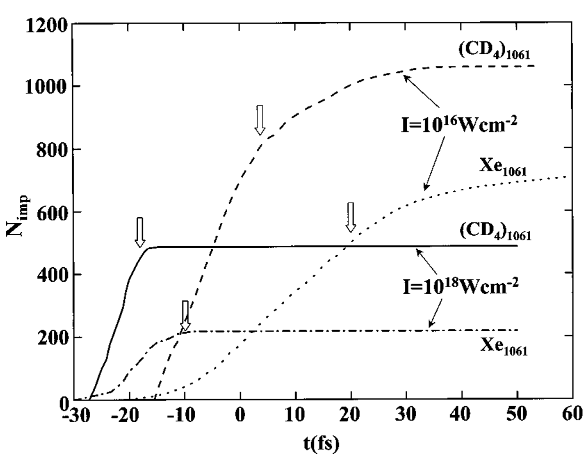

FIG. 4. The time dependence of the total number of electrons produced by impact ionization in $(CD_4)_{1061}$ and Xe_{1061} clusters at laser peak intensities of 10^{16} W cm^{-2} and of 10^{18} W cm^{-2} (marked on the curves). The vertical arrows represent the t_{ii} data for the near saturation of the inner ionization for each case.

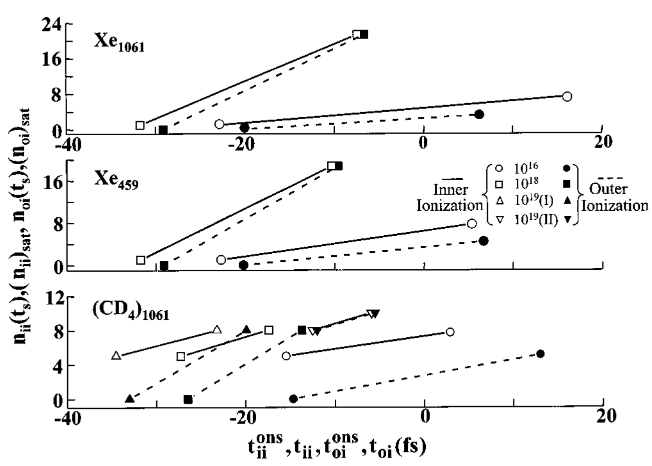

FIG. 5. A representation of initial levels and saturation levels for inner and outer ionization, together with the times (on the temporal scale of the laser pulse) for the onset and saturation for inner and outer ionization in molecular clusters. The open symbols represent inner ionization data with each solid line (——) connecting two points corresponding to $[t_{ii}^{ons},n_{ii}(t_s)]$ and $[t_{ii},(n_{ii})_{sat}]$, at the laser peak intensities of 10^{16} W cm^{-2} (○), 10^{18} W cm^{-2} (□), $I=10^{19}$ W cm^{-2} for the C^{+4} formation (△), and $I=10^{19}$ W cm^{-2} for the C^{+6} formation (▽). The closed symbols represent outer ionization data with each dashed line connecting two points $[t_{oi}^{ons},n_{oi}(t_s)]$ and $[t_{oi},(n_{oi})_{sat}]$ at the laser peak intensities of $I=10^{16}$ W cm^{-2} (●), $I=10^{18}$ W cm^{-2} (■), and $I=10^{19}$ W cm^{-2} with the formation of C^{+4} (▲) and $I=10^{19}$ W cm^{-2} with the formation of C^{+6} (▼). Lower panel: Xe_{459} and upper panel: Xe_{1061}.

$t_{ii}=2.9$ fs for $I=10^{16}$ W cm^{-2} and at $t_{ii}=-17.4$ fs for 10^{18} W cm^{-2}. On the other hand, at an even higher intensity of $I=10^{19}$ W cm^{-2} the inner ionization level of $(CD_4)_{459}$ manifests two steps (Figs. 1 and 5 and Table I), first increasing to $(n_{ii})_{sat}=8$ (marking the formation of $C^{4+}D_4^+$), saturating at $t_{ii}=-23.2$ fs and subsequently increasing to $(n_{ii})_{sat}=10$ (marking the additional ionization of the $(1s)^2$ inner shell and formation of $C^{6+}D_4^+$), with the saturation time at $t_{ii}=-5.9$ fs. For the lowest intensity of $I=10^{16}$ W cm^{-2}, the long (positive) values of t_{ii} and t_{oi} (Fig. 5) reflect that the most effective processes of inner/outer ionization occur in the vicinity of the laser field peak and beyond it. On the other hand, at higher intensities of $I=10^{18}$–10^{19} W cm^{-2} the negative t_{ii} values (Fig. 5) indicate that the valence electrons are ionized before the laser peak is attained, while the BSI of the inner shell $C(1s^2)$ electrons is accomplished at $I=10^{19}$ W cm^{-2} near the laser peak. The outer ionization level of $(CD_4)_{1061}$ at the lower intensity of $I=10^{16}$ W cm^{-2} reaches a limiting value of $(n_{oi})_{sat}=5.1$ at the outer ionization saturation time of $t_{oi}=-13.7$ fs (Figs. 1 and 5 and Table I). Thus, at $I=10^{16}$ W cm^{-2}, $(n_{oi})_{sat}<(n_{ii})_{sat}$ and $(n_p)_{sat}=2.6$ electrons remain in the nanoplasma. In contrast, at higher intensities of $I=10^{18}$–10^{19} W cm^{-2}, the inner and the outer saturation times are short and nearly equal, i.e., $t_{ii}\simeq t_{oi}\simeq -12$ fs for the ''one-step'' multielectron ionization at $I=10^{18}$ W cm^{-2} to $(n_{ii})_{sat}=8$, and $t_{ii}\simeq t_{oi}=-2$ fs for the two-step multielectron ionization to $(n_{ii})_{sat}=10$ at $I=10^{19}$ W cm^{-2}. Thus in the 10^{18}–10^{19} intensity domain $(n_{oi})_{sat}=(n_{ii})_{sat}$, and $(n_p)_{sat}=0$, manifesting complete nanoplasma depletion via outer ionization at relatively short times in the vicinity of the laser peak.

The inner and the outer ionization dynamics of Xe_n ($n=459$,1061) clusters for the peak intensities $I=10^{16}$ W cm^{-2} and 10^{18} W cm^{-2} are portrayed in Figs. 2 and 3. The onsets for inner/outer ionization for both Xe_{459} and Xe_{1061} clusters reflect the relation $t_{ii}^{ons}<t_{oi}^{ons}$, and are in accord with the sequential nature of the inner/outer ionization processes (Fig. 4). The same pattern is manifested for the $(CD_4)_{1061}$ clusters (Fig. 4). At rather low laser fields, i.e., at $t=-22$ fs for $I=10^{16}$ W cm^{-2} and at $t=-32$ fs for $I=10^{18}$ W cm^{-2}, a step in the inner ionization level from $n_{ii}=1$ to $n_{ii}=3$ is exhibited for Xe_{459} and Xe_{1061} (Figs. 2 and 3) at both intensities studied herein, which manifests sequential two electron field ionization with the formation of Xe^{3+}. A subsequent large increase of the ionization level occurs at longer times with increasing the field amplitude of the Gaussian pulse. In general, the saturation times t_{ii} exhibit a weak cluster size dependence and a marked intensity dependence for inner and for outer ionization (Fig. 5). At the lower intensity of $I=10^{16}$ W cm^{-2} the saturation levels for both inner and outer ionizations are manifested beyond the peak intensity (Figs. 2 and 5) with $t_{ii}=5.4$ fs and $t_{oi}=6.7$ fs for Xe_{459} (Fig. 4). At a higher intensity of $I=10^{18}$ W cm^{-2} the saturation times are somewhat below the laser field peak (Figs. 3 and 5) in the range $t_{ii}=-10.3$ fs and $t_{oi}=-9.6$ fs for Xe_{459} (Fig. 5). The difference between the ionization dynamics in $(Xe)_{1061}$ and $(CD_4)_{1061}$ clusters at both $I=10^{16}$ and 10^{18} W cm^{-2} is reflected in the appearance of longer saturation times for inner ionization in the former case (Figs. 1 and 3), i.e., $t_{ii}=6.2$ fs for Xe_{1061} and $t_{ii}=2.9$ fs for $(CD_4)_{1061}$ at $I=10^{16}$ W cm^{-2}, while $t_{ii}=-7.4$ fs for Xe_{1061} and $t_{ii}=-18$ fs for $(CD_4)_{1061}$ at $I=10^{18}$ W cm^{-2} (Fig. 5). This difference can be traced to the differences in the energetic hierarchy of the ionization potentials of a Xe atom and of a CD_4 molecule (Fig. 2 and Table I of Paper I). In the case of the CD_4 molecules, the ionization level $n_{ii}=8$ ($C^{4+}D_4^+$ ion) is attained at $I\sim 2\times 10^{16}$ W cm^{-2} and cannot be changed up to $I\sim 4\times 10^{18}$ W cm^{-2} [Fig. 2(a) of Paper I]. This is the reason for the broad saturation level in the ionization process generated for $(CD_4)_{1061}$ by the Gaussian shaped laser pulse (Fig. 1). In contrast, the ionization level of the Xe^{k+} ion increases more or less smoothly with increasing the laser field [Fig. 2(b) of Paper I], so that in the Xe_n clusters subjected to the Gaussian shaped laser pulse the inner ionization level also increases smoothly, up to the saturation level reached in the vicinity of the peak intensity (Figs. 2 and 3). The outer ionization level n_{oi} follows the inner ionization level n_{ii} (Sec. III).

The electron yields for the inner and for the outer ionization processes in Xe_n clusters (Figs. 2 and 3 and Table I) reveal a qualitative difference between the lower and the higher intensity regimes. At $I=10^{16}$ W cm^{-2} the asymptotic values of the ionization levels are $(n_{ii})_{sat}>(n_{oi})_{sat}$ (Table I), reflecting on the retention of the nanoplasma within the cluster with an asymptotic value of $(n_p)_{sat}=3.3$–4.0 for the nanoplasma population at ''long'' times of >30 fs (Fig. 2). On the other hand, for the higher intensity of $I=10^{18}$ W cm^{-2}, the nanoplasma is depleted at the time of $t>-5$ fs, where $(n_{ii})_{sat}=(n_{io})_{sat}$ and $(n_p)_{sat}=0$. The intensity dependent ionization level, with $(n_p)_{sat}$ being finite at $I=10^{16}$ W cm^{-1} and vanishing at $I=10^{18}$ W cm^{-2}, is qualitatively similar for Xe_n and $(CD_4)_n$ clusters.

E. Electron energies at the outer ionization spatial onset

A rough estimate was obtained from our simulations on the energetics of the electrons produced by outer ionization. In our simulations we have set the spatial limit for outer ionization as $r\geqslant 6R$. At the distance of $r=6R$, which corresponds to the outer ionization onset, our simulations for Xe_n ($n=249$–2171) in the intensity range $I=10^{16}$–10^{18} W cm^{-2} give average electron energies in the range of 1–40 keV. The average electron energies $\overline{\epsilon}_{av}$ at the spatial outer ionization onset for $I=10^{16}$ W cm^{-2} are $\overline{\epsilon}_{av}=1.18$ keV for Xe_{249}, $\overline{\epsilon}_{av}=1.39$ keV for Xe_{459}, and $\overline{\epsilon}_{av}=1.55$ keV for Xe_{1061}, while for $I=10^{18}$ W cm^{-2} $\overline{\epsilon}_{av}=10.1$ keV for Xe_{249}, $\overline{\epsilon}_{av}=14.1$ keV for Xe_{459}, $\overline{\epsilon}_{av}=25.7$ keV for Xe_{1061}, and $\overline{\epsilon}_{av}=39.6$ keV for Xe_{2171}. Thus $\overline{\epsilon}_{av}$ increases with increasing the cluster size and markedly increases with increasing the laser intensity. These results should be considered as approximate estimates only, as these $\overline{\epsilon}_{av}$ values (obtained at $r=6R$) do not reach saturation with a further increase of r (i.e., $\overline{\epsilon}_{av}$ increases by about 50% when r is further increased from $6R$ to $15R$). These simulation energetic data for the electron energies in the outer ionization of a single cluster cannot be directly confronted with experiment, where the energetics of the outer ionization of a single cluster cannot be interrogated, but rather the electrons are removed from the clusters into a macroscopic plasma (Sec. IV). At $I=10^{18}\,\mathrm{W\,cm^{-2}}$ the electron energies $\overline{\epsilon}_{av}$ correspond to velocities of $\sim$900–1200 Å fs^{-1}, which are not much smaller than the light velocity c ($v/c\sim0.3$–0.4). This finding confirms the need for our relativistic treatment of the motion of the electrons (Sec. II A).

III. ELECTRON DYNAMICS IN INNER AND OUTER IONIZATION

To specify further the electron dynamics, we introduce the half lifetimes $t_{ii}^{(1/2)}$ and $t_{oi}^{(1/2)}$ for inner and outer ionization, respectively, which characterize the attainment of 50% of the corresponding ionization process. These half lifetimes are obtained from the initial and final ionization levels in terms of the relations

$$n_{ii}(t_{ii}^{(1/2)})=[(n_{ii})_{sat}-n_{ii}(t_s)]/2,$$
$$n_{oi}(t_{oi}^{(1/2)})=(n_{oi})_{sat}/2. \quad (4)$$

The values of $t_{ii}^{(1/2)}$ and $t_{oi}^{(1/2)}$ can be inferred from the data of Figs. 1–3. The values of $t_{ii}^{(1/2)}$ and $t_{oi}^{(1/2)}$ are, of course, determined on the time-dependent laser field. Of interest is the delay time $\Delta\tau_{OI}$ between the half lifetimes for outer and for inner ionization

$$\Delta\tau_{OI}=t_{oi}^{(1/2)}-t_{ii}^{(1/2)}, \quad (5)$$

which provides a quantification of the relative time scales for the two basic ionization mechanisms. From the $\Delta\tau_{OI}$ data summarized in Table I for $(CD_4)_{1061}$ and Xe_n ($n=459$,1061) clusters, we infer that:

(1) For all the molecular clusters studied herein $\Delta\tau_{OI}>0$. The positive delay time demonstrates that the inner and the outer ionization processes are sequential, with the inner ionization preceding the outer ionization.

(2) $\Delta\tau_{OI}$ decreases with increasing the laser peak intensity.

(3) Some further indications are obtained for the sequential nature of the inner/outer ionization processes from the saturation times t_{ii} and t_{oi}. For $(CD_4)_{1061}$ clusters over the entire intensity domain (10^{16}–$10^{19}\,\mathrm{W\,cm^{-2}}$), for Xe_{459} clusters in the intensity domain of $I=10^{16}$–$10^{18}\,\mathrm{W\,cm^{-2}}$, and for Xe_{1061} in the intensity domain of $I=10^{18}\,\mathrm{W\,cm^{-2}}$, the data of Figs. 1 and 2 reveal that $t_{ii}<t_{oi}$, as appropriate for a sequential process. On the other hand, for the larger Xe_{1061} clusters at $I=10^{16}\,\mathrm{W\,cm^{-2}}$, this relation is not obeyed, reflecting on high-order hierarchical ionization of the Xe atoms in the cluster. Concurrently, the $\Delta\tau_{OI}$ data [point (1)] provide the necessary evidence for the (positive) time delay between the outer and the inner ionization of the sequentiality of these two basic, distinct processes.

To further specify electron dynamics in this laser-electron coupled system, we introduce the characteristic times τ_{ii} for inner ionization and τ_{oi} for outer ionization, which are defined as the lifetimes for the attainment of half of the limiting values for the inner/outer ionization, relative to t_{ii} and to t_{oi}, respectively. The characteristic times are given by the relations

$$\tau_{ii}=t_{ii}-t_{ii}^{(1/2)}, \quad \tau_{oi}=t_{oi}-t_{oi}^{(1/2)}. \quad (6)$$

The characteristic time τ_{ii} corresponds to the time scale for the nanoplasma formation (to be further discussed in Sec. IV), while τ_{oi} represents the depletion time of the nanoplasma.

The characteristic times for $(CD_4)_{1061}$ clusters (Table I) were obtained from the simulations of the electron dynamics (Fig. 1). These characteristic times in the intensity range 10^{16}–$10^{18}\,\mathrm{W\,cm^{-2}}$ vary in the region 9–2 fs for τ_{ii} and 15–4 fs for τ_{oi}, revealing the decrease of both τ_{ii} and τ_{oi} with increasing the laser intensity (Table I), as expected for the barrier suppression ionization mechanism for inner ionization[24] of the cluster constituents, and the cluster barrier suppression mechanism for outer ionization (Paper I). At the lower intensity of $I=10^{16}\,\mathrm{W\,cm^{-2}}$, $\tau_{ii}<\tau_{oi}$, pointing towards sequential inner/outer ionization dynamics. At $I=10^{16}\,\mathrm{W\,cm^{-2}}$ the retardation of the outer ionization dynamics reflects on the retention of the nanoplasma within the cluster for long times, which provides a screening effect. In this intensity range the values of $\tau_{oi}\simeq15.2$ fs and $\tau_{ii}=9$ fs are comparable to the laser pulse width of 18 fs. At higher intensities of 10^{18}–$10^{19}\,\mathrm{W\,cm^{-2}}$, the characteristic times τ_{ii} and τ_{oi} in the range of 3–4 fs (Table I) are considerably shorter than the pulse width. For these higher intensities $\tau_{ii}\simeq\tau_{oi}$ (or rather $\tau_{ii}\lesssim\tau_{oi}$,) with the time scale for a complete electron depletion from the nanoplasma being close to the time scale for the nanoplasma formation in these clusters.

The characteristic times for Xe_n clusters in the intensity range $I=10^{16}$–$10^{18}\,\mathrm{W\,cm^{-2}}$ (Table I) fall in the range $\tau_{ii}=30$–7 fs and $\tau_{oi}=13$–5 fs. The femtosecond time range for electron dynamics in Xe_n clusters is qualitatively similar to that in $(CD_4)_n$ clusters, however, some quantitative differences prevail. In Xe_n clusters, both τ_{ii} and τ_{oi} decrease with increasing the laser peak intensity, as in the case for $(CD_4)_{1061}$ clusters, in accord with the BSI mechanism for inner ionization of the constituents and the cluster barrier suppression ionization mechanism for outer ionization (Paper I). For the $(CD_4)_{1061}$ cluster $\tau_{ii}<\tau_{oi}$, as appropriate for the sequential inner–outer ionization dynamics [point (1)]. In contrast, for Xe_n clusters, the inverted relation $\tau_{ii}>\tau_{oi}$ prevails. This difference reflects on the energetic hierarchy in the ionization potential of the Xe atoms, already referred to above in the context of the saturation times (Sec. II D).

Of interest are some manifestations of the oscillatory behavior of the ionization levels induced by the interaction with the laser field. Both inner and outer ionization levels, as well as the nanoplasma population in Xe_n clusters at high intensities ($I=10^{18}\,\mathrm{W\,cm^{-2}}$), exhibit temporal oscillations (Fig. 3) with a frequency that equals the double value of the laser frequency. The maxima of the temporal oscillations in n_{ii}, n_{oi}, and n_p roughly coincide with the maxima of the laser field amplitudes, in accord with the physical model of field ionization of the constituents (Paper I).

Subsequent and parallel to the outer ionization process, which results in cluster charging, the Coulomb explosion process sets in. The nuclear, ionic Coulomb expansion affects the electronic inner and outer ionization processes.[13,27] The time scales for Coulomb explosion, which are characterized by the time of the cluster radius doubling, fall in the range of $\tau_{CE}=10-20$ fs.[10,13–15,23] These time scales for τ_{CE} nuclear dynamics are comparable to the characteristic times τ_{ii} and τ_{oi} for the electron dynamics for inner/outer ionization at $I=10^{16}\,\mathrm{W\,cm^{-2}}$ (Table I), while at $I=10^{18}\,\mathrm{W\,cm^{-2}}$ the time scales for nuclear dynamics are longer than those for electron inner/outer ionization dynamics (Table I). The coupling between the electronic ionization dynamics and the nuclear Coulomb explosion dynamics, whose consequences were explored herein by our simulations, may be of some importance and requires further study.[27]

IV. NANOPLASMA

The unbound electrons generated by inner ionization, which are confined to the cluster and to its vicinity, and the cluster ions form the nanoplasma. With the onset of the laser pulse, the number of unbound electrons in the plasma, $N_e=nn_p$ (with $n_p=n_{ii}-n_{oi}$) first increases and subsequently either reaches saturation for lower intensities of $I=10^{16}\,\mathrm{W\,cm^{-2}}$ (Figs. 1 and 2) or is completely depleted at $I=10^{18}\,\mathrm{W\,cm^{-2}}$ (Fig. 3).

At this point it will be appropriate to distinguish between the nanoplasma in single clusters and a macroplasma (with the size of $\sim 10^{-3}-10^{-1}$ cm) formed in a cluster beam within the laser focus (the plasma filament).[7,17] The formation of this macroplasma starts with the onset of the outer ionization process, which transfers the cluster electrons to the intercluster space. At the high laser intensity of $I=10^{18}\,\mathrm{W\,cm^{-2}}$ the outer ionization process removes all the cluster electrons (Figs. 1 and 3), thus completing the formation of the plasma filament. The situation is different at the lower laser intensity of $I=10^{16}\,\mathrm{W\,cm^{-2}}$ when the cluster plasma continues to exist after the outer ionization process reaches saturation $(n_p)_{sat}>0$ (Figs. 1 and 2). In this case, the plasma filament is formed in two steps. The first step involves the outer ionization process on the time scale of 20–30 fs (Figs. 1 and 2). The second step takes place when, due to Coulomb explosion, the cluster diameters become comparable to the intercluster distances, so that the identification of single clusters loses its significance and the cluster electrons constitute the electrons of the plasma filament. This process is realized some 100–200 fs after the onset of the cluster ionization process.[7,15]

We shall now return to the properties and dynamic response of the nanoplasma interacting with the laser field. The following properties of nanoplasma are notable:

(1) The nanoplasma is positively charged. As $n_{ii}(t)>n_p(t)$ for all t (Figs. 1–3), the nanoplasma is positively charged. The total positive charge of the nanoplasma is $Q(t)=n[n_{ii}(t)-n_p(t)]=nn_{oi}(t)$, provided that $n_p(t)>0$.

(2) Persistent $[(n_p)_{sat}>0]$ and transient $[(n_p)_{sat}=0]$ nanoplasma in $(CD_4)_{1061}$ and in Xe_n ($n=1061,459$) clusters. The persistent nanoplasma prevails at the lower intensity of $I=10^{16}\,\mathrm{W\,cm^{-2}}$, while in the higher intensity domain of $I=10^{18}-10^{19}\,\mathrm{W\,cm^{-2}}$ the existence of the transient nanoplasma is realized.

(3) Femtosecond time scales for the nanoplasma formation and depletion.

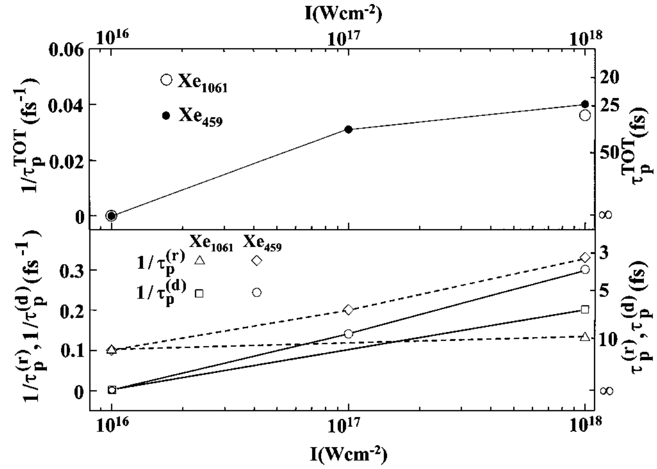

FIG. 6. Time evolution of the electron populations of the nanoplasma in Xe_{459} and Xe_{1061} clusters in the laser peak intensity domain $I=10^{16}-10^{18}\,\mathrm{W\,cm^{-2}}$. The upper panel represents the reciprocal values of the nanoplasma temporal width $(\tau_p^{(d)})^{-1}$, while the lower panel represents the reciprocal values of the rise time $(\tau_p^{(r)})^{-1}$ and the decay time $(\tau_p^{(d)})^{-1}$. At the lowest intensity of $I=10^{16}\,\mathrm{W\,cm^{-2}}$ the nanoplasma is persistent with $(\tau_p^{\mathrm{TOT}})^{-1}\simeq 0$ and $(\tau_p^{(d)})^{-1}\simeq 0$. The lines combining the points (specified on the figure) are drawn to guide the eye.

The time evolution of the electron population of the nanoplasma is characterized by the total temporal width τ_p^{TOT} [the time delay between the onset and the vanishing of $n_p(t)$], the nanoplasma rise time $\tau_p^{(r)}$ [the time difference between the times corresponding to the attainment of $(n_p)_{sat}$ and of $(n_p)_{sat}/2$ on the rising part of $n_p(t)$], and the nanopolasma decay time $\tau_p^{(d)}$ [the difference between the times corresponding to $(n_p)_{sat/2}$ and of $(n_p)_{sat}$ on the falling part of $n_p(t)$]. In Fig. 6 we present these nanoplasma characteristic lifetimes τ_p^{TOT}, $\tau_p^{(r)}$, and $\tau_{pd}^{(d)}$ [where the oscillatory behavior of $n_p(t)$ was averaged out]. For the laser pulse used herein, the τ_p^{TOT} values, which are finite for $I>10^{16}\,\mathrm{W\,cm^{-2}}$, fall in the range 10–30 fs, and the $\tau_p^{(d)}$ lifetimes can be defined in this intensity domain (Fig. 6). The characteristic lifetimes for the nanoplasma risetime $\tau_p^{(r)}$ (for all the I values studied herein) fall in the 3–10 fs time domain, exhibiting a weak cluster size dependence and decrease with increasing I. The nanoplasma decay times $\tau_p^{(d)}$ (for $I>10^{16}\,\mathrm{W\,cm^{-2}}$) fall in the range 3–7 fs and decrease with increasing I. At the lower intensity of $I=10^{16}\,\mathrm{W\,cm^{-2}}$ the nanoplasma population persists over "long" times of >50 fs. The lifetime of the nanoplasma under these conditions is expected to be $\sim$100–200 fs,[7,15] as previously discussed.

Information on the spatial inhomogeneity and dynamics of response of the nanoplasma emerges from snapshots of spatial distribution of the unbound electrons at different times. The snapshots for Xe_n clusters at $I=10^{16}\,\mathrm{W\,cm^{-2}}$ (Fig. 7) show that the electron cloud is spatially inhomogeneous, while the majority of the unbound electrons are located inside the cluster. At those times, in the vicinity of the peak of the laser pulse, the plasma electrons are subjected to temporal oscillations and the electron cloud becomes slightly elongated along the polarization direction of the laser field $\vec{F}_\ell$ [Fig. 7(a)]. With the decrease of the laser field at $t>0$ the electron oscillations become weaker [Fig. 7(b)]. Simul-

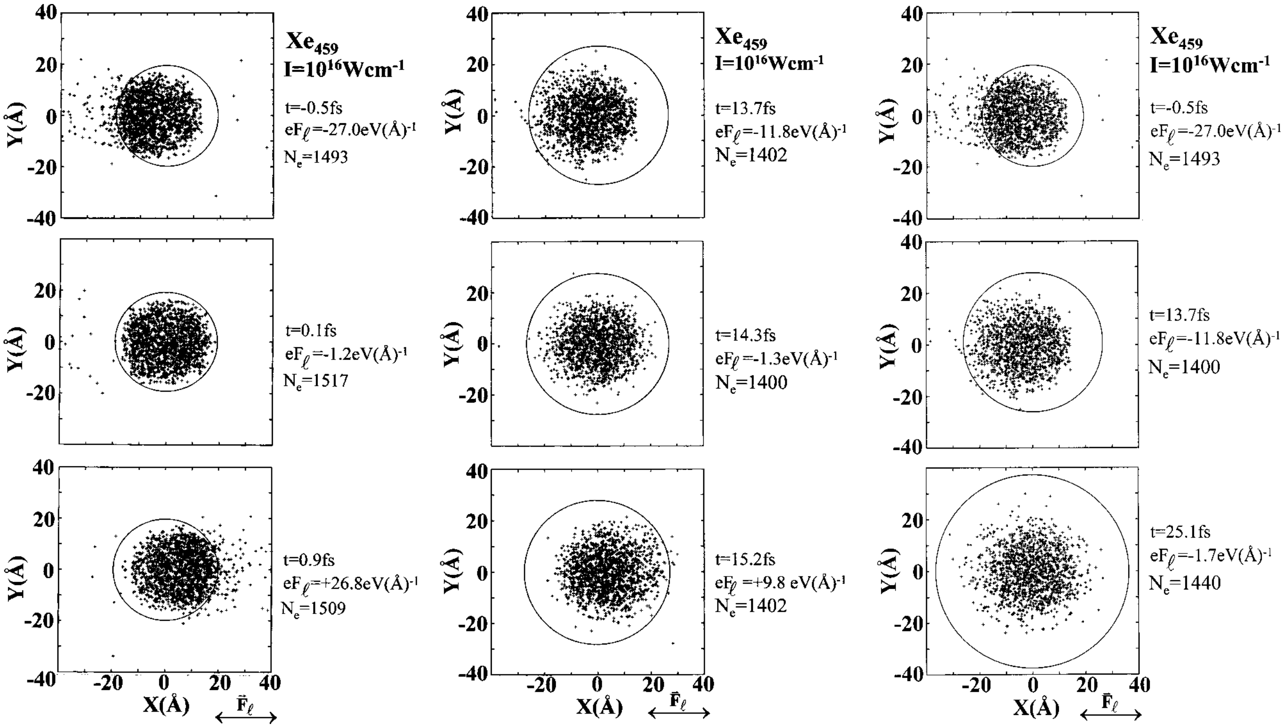

FIG. 7. The dynamics of the electron cloud in the nanoplasma (represented in two dimensions) in a Xe_{459} cluster at the laser intensity $I=10^{16}$ W cm^{-2} and propagation direction along the *x* axis, as obtained from molecular dynamics simulations (see text). The numbers represent the time *t* (on the time scale of the laser pulse) and the laser field eF_{ℓ} (in eV Å^{-1}). The total number of electrons N_e is presented on the figures. The circles represent the cluster size. (a) The electron cloud (nanoplasma) oscillating in the temporal vicinity of the peak of the laser field, exhibiting a left-side/right-side biased distribution at $t=-0.5$ fs/0.9 fs, when $eF_{\ell}=-27$ eV Å^{-1}/26.8 eV Å^{-1} and a central distribution at $t=0.9$ fs for a low $eF_{\ell}=-1.2$ eV Å value. (b) Subsequent time events, when the cluster manifests Coulomb explosion while the electron cloud (nanoplasma) continues to exhibit oscillatory behavior in the laser field, exhibiting a left-side/right-side biased distorted distribution at 13.7 fs/15.2 fs, when $eF_{\ell}=-11.8$ eV Å^{-1}/9.8 eV Å^{-1} and a central distribution at $t=14.3$ fs for a low $eF_{\ell}=-1.3$ eV Å^{-1} value. (c) Left-side biased distributions for three different stages of Coulomb explosion: (i) $t=-0.5$ fs, cluster radius *R* close to the initial radius R_0, with the laser intensity at maximum; (ii) $t=13.7$ fs, $R\approx 1.4R_0$, with the laser intensity; and (iii) $t=25.1$ fs, $R\approx 2R_0$, with the laser intensity being close to zero.

taneously with the laser field decrease, the radius of the Coulomb exploding cluster increases [Fig. 7(c)], and finally the electron cloud becomes symmetrical and concentrated mainly around the cluster center. At the laser intensity $I=10^{18}$ W cm^{-2} the spatial inhomogeneity of temporal oscillations are very strong (Fig. 8). When the number of electrons is large [Fig. 8(a)] the electron cloud is strongly elongated along $\vec{F}_{\ell}$, at least in the vicinity of the laser field amplitudes. The laser field moves electrons through the cluster when the direction of the field is changed, and at the laser field peak amplitudes a significant fraction of electrons is shifted out from the cluster. When the number of the unbound electrons becomes small and the laser field becomes stronger, the electrons move mostly outside the clusters [Fig. 8(b)] and outer ionization prevails. At $I=10^{18}$ W cm^{-2} the electrons outside the cluster move mostly along the *x*-coordinate but with some small shift towards the positive *z*-direction, i.e., the direction of the laser light propagation (Fig. 8). This shift is due to the magnetic component of the laser light field (included in our simulations[25]), indicating that the electron velocity outside the cluster is not negligibly small as compared to the light velocity and confirming the need for the relativistic approach used in the dynamic simulations.

The snapshots of the electron oscillations in the outer part of the nanoplasma are clearly represented in Fig. 9, where the oscillatory motion of the electron center of mass X_{CM} along the laser field $\vec{F}_{\ell}$ direction (the *x*-axes) is shown for the Xe_{459} cluster subjected to the laser pulse peak intensity $I=10^{17}$ W cm^{-2}. The process of energy pumping from the laser field to the nanoplasma, and consequently the outer ionization process, can be enhanced by the quasiresonance mechanism. The quasiresonance character of the energy pumping is manifested by the oscillations of the center of mass X_{CM} of the unbound electrons along the laser field $\vec{F}_{\ell}$ polarization direction. The temporal onset of the population of the nanoplasma (per Xe atom) increases from the initial value of unity to a maximal value of 3.5 at $t\sim-10$ fs and decreases to zero at $t\sim5$ fs (Fig. 9). The weak oscillations in the population of the nanoplasma, with a frequency which corresponds to the double value of the laser frequency (Fig. 9), are in accord with the results for higher intensities (Fig. 3 and Sec. II D). According to Fig. 9 the X_{CM} demonstrates strong oscillations with the amplitude comparable at $t>-15$ fs to the cluster radius which is initially $R_0=18.4$ Å, and $R=20$ Å and $R=30$ Å at $t=-10$ fs and $t=0$, respectively. The phase shift between the laser field and the X_{CM} oscillations increases in time, being $\sim0.2\pi$ at $t=-10$ fs and ~0.4–0.5π in the vicinity of the pulse peak at $t=0$. The phase shift indicates a contribution of a quasiresonance process to the energy pumping from the laser field to

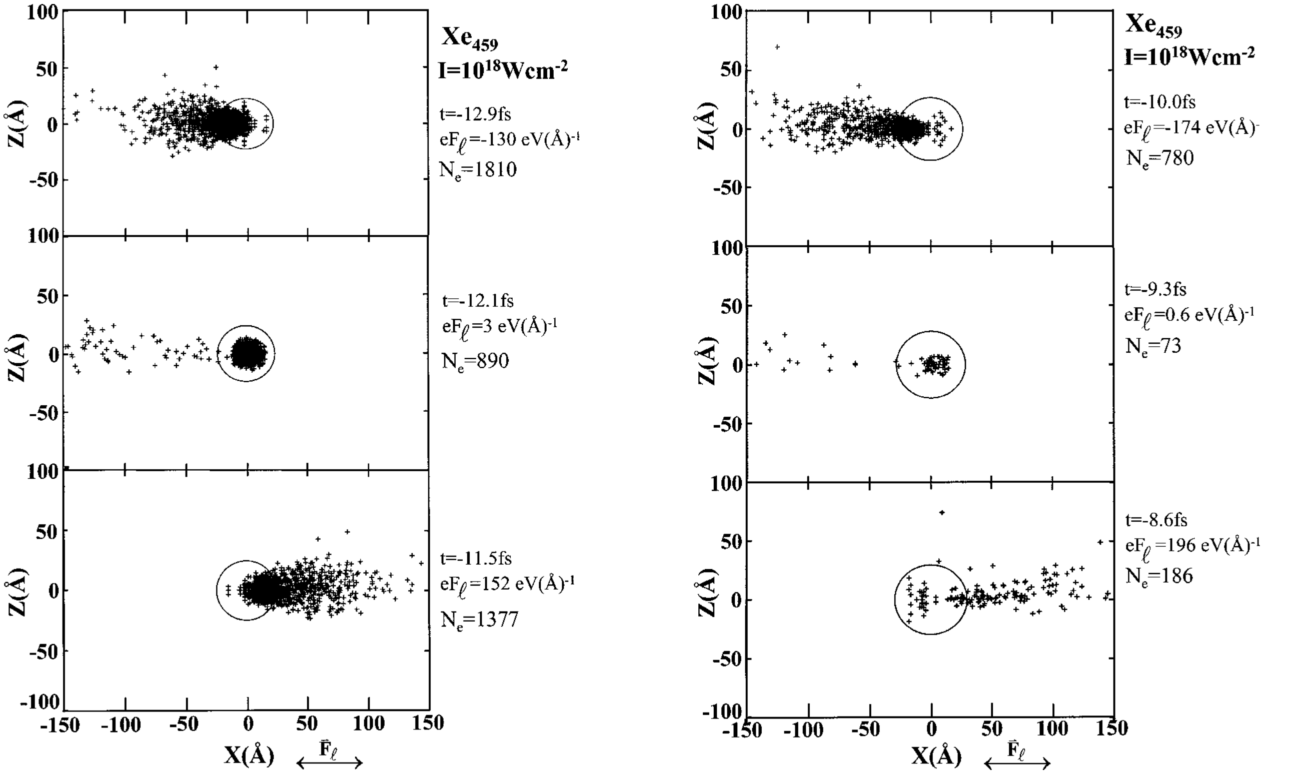

FIG. 8. The dynamics of the electron cloud in the nanoplasma (represented in two dimensions) in Xe_{459} clusters at the high laser intensity of $I=10^{18}\,\mathrm{W\,cm^{-2}}$, obtained from molecular dynamics simulations (see text). The circles represent the cluster size. Notations as in Fig. 7. The laser field is polarized along the z axis and the direction of the light propagation is along the z axis. The simulations represent oscillatory time dependence of the electron cloud in the laser field exhibiting left-side/right-side biased distribution at large $|eF_\ell|$ values and a central distribution for low $|eF_\ell|$. (a) Early time events $t=-12.9$ to -11.5 fs, with an oscillatory laser driven electron cloud. Note the large values of $N_e=1810$–890. (b) Later time events $t=-10.0$ to -8.6 fs. Increase of size of electron cloud during oscillatory laser driving. Note lowering of Ne to $N_e=780$–186 due to outer ionization. Small asymmetry along the z axis originates from magnetic field effects.

the cluster electrons. Concurrently, with the increase of the laser field, the quasiresonance effect drives the outer ionization, which is nearly complete, just above the peak of the laser field (Fig. 9).

Some further information emerges from the simulations of the spatial, angular and energetic distribution of the electrons within the nanoplasma. In what follows, typical results are presented for Xe_{1061} clusters in the laser peak intensity range 10^{16}–$10^{18}\,\mathrm{W\,cm^{-2}}$. Figures 10 and 11 display the radial spatial distribution probability $P(r/R)$ of the electrons at their distances r from the cluster centers (normalized to the cluster radius R), together with the electrons' average energy ϵ_{av} at r/R. The $P(r/R)$ and $\epsilon_{av}(r/R)$ spatial distributions are presented for several laser fields (F_ℓ) at a fixed laser peak intensity I. For the lower peak intensity of $I=10^{16}\,\mathrm{W\,cm^{-2}}$, the $P(r/R)$ curves for both laser fields $F_\ell=-27\,\mathrm{eV\,Å^{-1}}$ and $F_\ell=6\,\mathrm{eV\,Å^{-1}}$ are qualitatively similar to the initial electron spatial distribution (Fig. 10), with a small deviation of the maximum towards a lower value of r/R. At the higher F_ℓ value a tail in the radial distribution towards larger values of $r/R>1$ is exhibited (Fig. 10), manifesting the displacement of the electron cloud, in accord with the snapshot for the spatial extension of the electron cloud beyond the cluster boundary [first and third panels in Fig. 7(a)]. At the high intensity range of $I\equiv 10^{18}\,\mathrm{W\,cm^{-2}}$ the $P(r/R)$ distribution (Fig. 10) is qualitatively different from the lower intensity domain. At $I=10^{18}\,\mathrm{W\,cm^{-2}}$ and low $F_\ell=-2\,\mathrm{eV\,Å^{-1}}$, a strong distortion of the spatial electron distribution from the initial distribution occurs toward low values of r/R (Fig. 11). This spatial shrinking of the electron cloud, which peaks in the vicinity of $r/R\simeq 0.3$, is caused by the enhanced electron–ion Coulomb attraction, which is due to the large ionic charge of the cluster ($Q_I\simeq 17\,000$) produced by the effective outer ionization in this intensity domain. For a strong laser field of $F_\ell=-17.4\,\mathrm{eV\,Å^{-1}}$, a wide $P(r/R)$ distribution peaking at $r/R\simeq 0.5$ with a broad spatial tail towards higher values of r/R is exhibited. The $P(r/R)$ curve extends well beyond the cluster boundary, in accord with the maps of the spatial electron distribution (Fig. 8).

The spatial distribution of the average energy (lower panels of Figs. 10 and 11) at $I=10^{16}\,\mathrm{W\,cm^{-2}}$ and $I=10^{18}\,\mathrm{W\,cm^{-2}}$ reveals a weak spatial dependence of $\epsilon_{av}(r/R)$ within the cluster at $r<R$. At $I=10^{16}\,\mathrm{W\,cm^{-2}}$, $\epsilon_{av}=50$–60 eV for $r<0.9R$ (Fig. 10), while at $I=10^{18}\,\mathrm{W\,cm^{-2}}$ $\epsilon_{av}=0.4$–0.9 keV for $r<R$ (Fig. 10). At a fixed value of I, the uniform average electron energy of the nanoplasma is nearly independent of F_ℓ, and increases (roughly as $I^{1/2}$) with increasing the laser peak intensity I. The average energy markedly increases when approaching the cluster boundary and beyond it. At $I=10^{16}\,\mathrm{W\,cm^{-2}}$ and $eF_\ell=-27\,\mathrm{eV\,Å^{-1}}$, ϵ_{av} increases to high values of ϵ_{av}

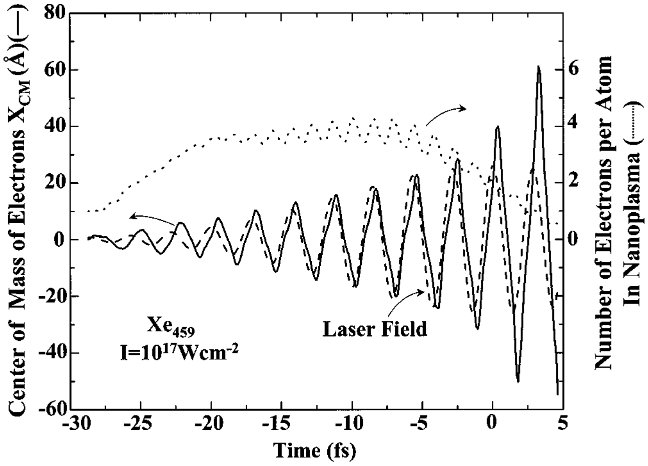

FIG. 9. Electron dynamics of outer ionization of $(Xe)_{459}$ clusters at $I=10^{17}$ W cm^{-2}. The time dependence of the laser field (in arbitrary units) is represented by a dashed line. The center of mass X_{CM} of the electron cloud along the light propagation direction (——) nearly follows the laser oscillations (see text), but exhibits an increase of the amplitude with increasing time due to outer ionization. The outer ionization is manifested by the decrease of the number of the electrons (per atom) in the cluster (right scale) with increasing time (· · · ·). The number of electrons shows oscillatory time dependence (with a doubled frequency of that of the laser field). The outer ionization time is ~5 fs under these conditions.

$\simeq 1000$ eV at $r/R=1.7$, while at $eF_\ell=6$ eV Å^{-1} the average energy reaches a peak of $\epsilon_{av}\simeq 400$ eV at $r/R=1.2$ (Fig. 10). At $I=10^{18}$ W cm^{-2} and at $eF_\ell=-174$ eV Å^{-1} the high-field increase of ϵ_{av} beyond the cluster boundary is exhibited to a value of $\epsilon_{av}\simeq 3$ keV at $r/R=1.7$. The increase of the ϵ_{av} values of the nanoplasma average energy beyond the cluster boundary towards the values 1–3 keV is in accord with the high keV values of the electron energies at $r=6R$, which were (arbitrarily) specified in Sec. II E as the onset of outer ionization.

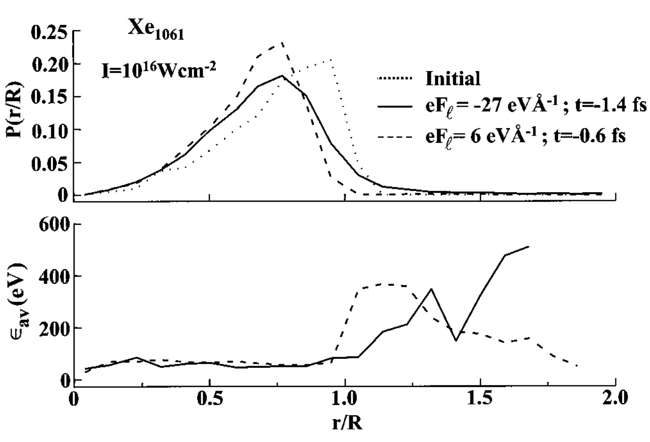

FIG. 10. Spatial radial distribution probability $P(r/R)$ of the nanoplasma electrons, where R is the cluster radius (upper panel) and spatial distribution of the electrons' average energy ϵ_{av} in a nanoplasma produced in a Xe_{1061} cluster by a laser field of peak intensity of $I=10^{16}$ W cm^{-2}. The data, which are recorded at a high laser field $eF_\ell=-27$ eV Å^{-1} (——) and at a low laser field $eF_\ell=6$ eV Å^{-1} (— — —), are marked on the curves together with the times t for the laser pulse. The initial radial electron distribution (at $t=t_s$, see text) is also shown on the upper panel. Note a small shift of the maximum of $P(r/R)$ towards lower r/R values and the increase of ϵ_{av} beyond the cluster boundary.

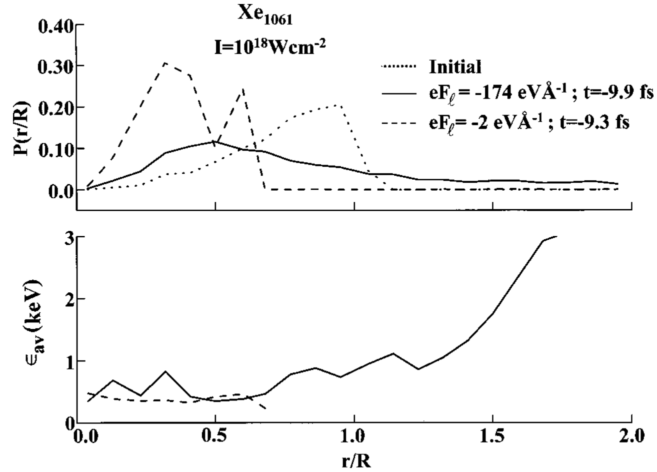

FIG. 11. Spatial radial distribution probability $P(r/R)$ of the nanoplasma electrons (upper panel) and spatial distribution of the electron average energy ϵ_{av} in a nanoplasma produced in a Xe_{1061} cluster by a laser field of peak intensity $I=10^{18}$ W cm^{-2}. The data, which are recorded at a high laser field of $eF_\ell=-174$ eV Å^{-1} (——) and at a low laser field of $eF_\ell=-2$ eV Å (— — —), are marked on the curves together with the times t for the laser pulse. The initial radial electron distribution (at $t=t_s$, see text) is also shown on the upper panel. Note the spatial shrinking of the spatial radial distribution due to electrostatic effects, the nearly constant ϵ_{av} within the cluster (the limited data range for the low field being due to a very low electron density beyond $r/R>0.7$), and the marked rise of ϵ_{av} beyond the cluster boundary.

The angular distribution $P(\theta)$ of the nanoplasma electrons (Figs. 12 and 13) from Xe_{1061} clusters is presented separately for the interior ($r<R$) and the exterior ($r>R$) spatial regimes. At the lower intensity of $I=10^{16}$ W cm^{-2} and a high (negative) field of $eF_\ell=-27$ eV Å^{-1}, the interior ($r<R$) angular distribution is similar to the "uniform" distribution $P(\theta)=\sin\theta$, which peaks at $\theta=\pi/2$ (Fig. 12). The exterior angular distribution is strongly biased toward large

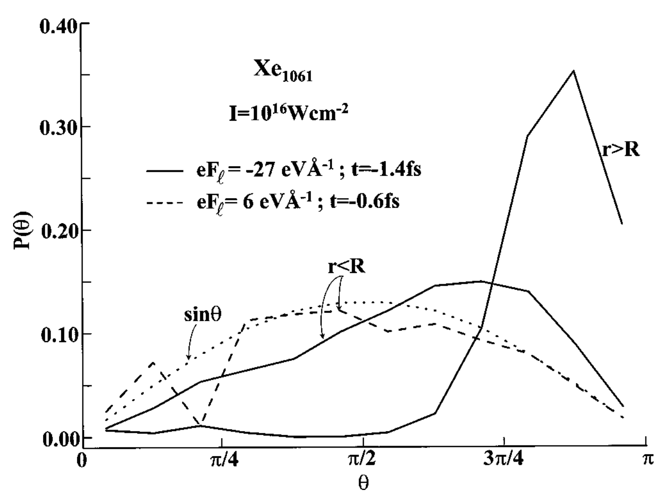

FIG. 12. The angular distribution $P(\theta)$ of the nanoplasma electrons produced in Xe_{1061} clusters by laser fields with a peak intensity of $I=10^{16}$ W cm^{-2}. The data, which are recorded at a high laser field of $eF_\ell=-27$ eV Å^{-1} (——) and at a low laser field of $eF_\ell=6$ eV Å^{-1} (— — —), are marked on the curves, together with the times t for the laser pulse. Data are presented for interior ($r<R$) and exterior ($r>R$) plasma electrons. A reference curve (· · · ·) $P(\theta)\propto\sin\theta$ for random angular distribution is also presented.

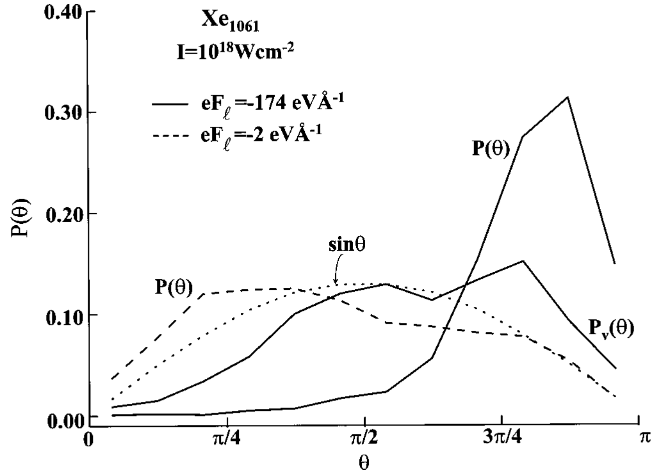

FIG. 13. The angular distribution $P(\theta)$ and the angular velocity distribution $P_v(\theta)$ of the nanoplasma electrons produced in a Xe_{1061} cluster by a laser peak intensity of $I=10^{18}\,W\,cm^{-2}$, at a high laser field of $eF_\ell=-174\,eV\,Å^{-1}$ (——) and at a low laser field of $eF_\ell=-2\,eV\,Å^{-1}$ (— — —). A reference curve (· · · ·) $P(\theta)\propto\sin\theta$ is also given.

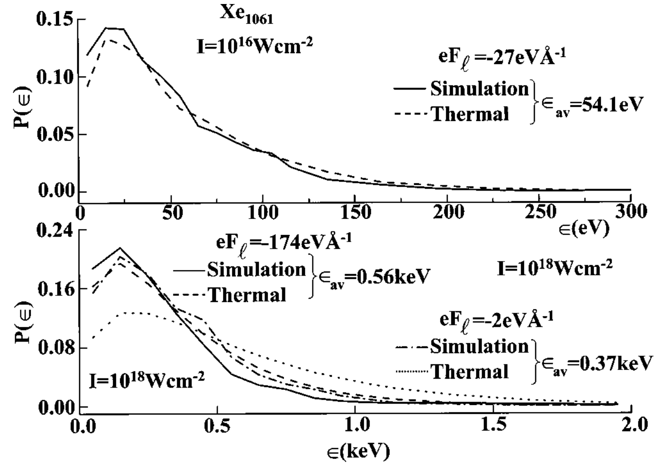

FIG. 14. Energy distribution in a nanoplasma produced in a Xe_{1061} cluster by a laser peak intensity of $I=10^{16}\,W\,cm^{-2}$ and a laser field of $eF_\ell=-27\,eV\,Å^{-1}$ (——), shown in the upper panel, and by a laser of peak intensity of $I=10^{18}\,W\,cm^{-2}$ and laser fields of $eF_\ell=-274\,eV\,Å^{-1}$ (——) and of $eF_\ell=-2\,eV\,Å^{-1}$ (—·—·—·—), shown in the lower panel. The simulation data (marked as "simulation") for $P(\epsilon)$ are fit by thermal distributions $P_T(\epsilon)$, Eq. (7) (marked as "thermal"), with the average energy (ϵ_{av}) calculated from the first moment of the simulated energy distributions. Upper panel: $I=10^{16}\,W\,cm^{-2}$ and high field $eF_\ell=-27\,eV\,Å^{-1}$. $P(\epsilon)$ is well fit by $P_T(\epsilon)$. Lower panel: $I=10^{18}\,W\,cm^{-2}$. There is a reasonably good fit for a high field $eF_\ell=-174\,eV\,Å^{-1}$ and a poor fit for a low field $eF_\ell=-2\,eV\,Å^{-1}$.

values of θ, peaking at $\theta=3\pi/4$ (Fig. 12), with the majority of the (small number of) exterior electrons being located in the field direction, as evident from the maps of the electron cloud in Fig. 8. A similar angular distribution is exhibited at a high intensity of $I=10^{18}\,W\,cm^{-2}$, where at a high negative field of $eF_\ell=-174\,eV\,Å^{-1}$, $P(\theta)$ manifests a marked angular bias for all the cluster electrons, with $P(\theta)$ peaking at $\sim7\pi/8$ and the majority of the electrons being located at a steroangle of $3\pi/4-\pi$ (Fig. 13). At this high intensity and at a weak field of $eF_\ell=-2\,eV\,Å^{-1}$, the angular distribution of $P(\theta)$ is similar to the "uniform" distribution, with a slight shift towards the lower θ values (Fig. 13). The strongly biased angular distribution at high $|eF_\ell|$ values, together with the nearly uniform distribution at low $|eF_\ell|$ values, is in accord with the electron cloud maps of Fig. 8. The data for the angular distributions shown in Figs. 12 and 13 are portrayed for negative (or low) values of eF_ℓ, while inverting the sign of eF_ℓ results in the inversion of the angular distribution with $\theta(\text{negative}\,eF_\ell)\rightarrow(\pi-\theta)(\text{positive}\,eF_\ell)$, as confirmed by our numerical simulations, which are not shown herein. The most interesting result emerging from the present analysis is the quantification of the angular anisotropy of the nanoplasma.

Additional information emerges for the angular distribution of the electron velocities $P_v(\theta)$, which are also presented in Fig. 13. At $I=10^{18}\,W\,cm^{-2}$ and (large) $eF_\ell=-174\,eV\,Å^{-1}$, the velocity angular distribution $P_v(\theta)$ is biased towards larger values of θ, as compared with the "uniform" distribution (Fig. 13), while for $eF_\ell=174\,eV\,Å^{-1}$ the bias occurs toward smaller values of θ (not shown here). Thus the velocity distribution within the nanoplasma is not random.

Of interest is the energy (ϵ) distribution $P(\epsilon)$ of the electrons in the nanoplasma (Fig. 14). From the simulation data for the (normalized) $P(\epsilon)$ distribution for $r\leqslant R$ at a fixed laser field for peak intensities of $I=10^{16}\,W\,cm^{-2}$ and $I=10^{18}\,W\,cm^{-2}$ (Fig. 14), we calculated the average electron energies $\epsilon_{av}=\int_0^\infty d\epsilon\,\epsilon P(\epsilon)$. The first moments of $P(\epsilon)$ resulted in $\epsilon_{av}=54.1\,eV$ at $I=10^{16}\,W\,cm^{-2}$ and $eF_\ell=-27\,(eV\,Å)^{-1}$, $\epsilon_{av}=0.56\,keV$ at $I=10^{18}\,W\,cm^{-2}$ and $eF_\ell=-174\,eV\,Å^{-1}$ and $\epsilon_{av}=0.37\,keV$ at $I=10^{18}\,W\,cm^{-2}$ and $eF_\ell=-2\,eV\,Å^{-1}$. The estimates of ϵ_{av}, at the higher intensity of $I=10^{18}\,W\,cm^{-2}$, are fraught with difficulty in view of the presence of a weak, high-energy tail, which gives a substantial (more than 20%) contribution of ϵ_{av}, while this effect is absent for the lower intensity of $I=10^{16}\,W\,cm^{-2}$. A cursory examination of the simulated $P(\epsilon)$ distributions at high and low fields at $I=10^{18}\,W\,cm^{-2}$ (lower panel of Fig. 14) for $eF_\ell=-174\,eV\,Å$ and for $eF_\ell=-2\,eV\,Å^{-1}$ reveals that these two energy distributions are quite similar in the intermediate energy range $\epsilon=0$–1.2 keV, however, their first moments differ by 40% due to the different contribution from the high energy tails of the distributions. In this context, it is interesting to use these ϵ_{av} data for the comparison of the simulated $P(\epsilon)$ with the thermal energy distribution $P_T(\epsilon)$, with an effective temperature $k_eT=2\epsilon2v/3$, which is given by

$$P_T(\epsilon)\propto(\epsilon/\epsilon_{av})^{1/2}\exp(-3\epsilon/2\epsilon_{av}). \tag{7}$$

We note in passing that Eq. (7) corresponds to a potential-free (or a constant potential) system. From the results of Fig. 14 it is apparent that at $I=10^{16}\,W\,cm^{-2}$ the thermal energy distribution [with $\epsilon_{av}=54.1\,eV$ obtained from the first moment of $P(\epsilon)$] fits well the simulation data at high laser fields of $eF_\ell=-27\,eV$. At $I=10^{18}\,W\,cm^{-2}$ again a reasonably good fit of the simulation data to the thermal distribution with $\epsilon_{av}=0.56\,keV$ is obtained at a high field of $eF_\ell=-174\,eV\,Å^{-1}$ (Fig. 14). However, marked deviations of the high field values of $P(\epsilon)$ from $P_T(\epsilon)$ are obtained in the energy range $\epsilon=0.4$–1.0 keV (Fig. 14). Furthermore, at

$I=10^{18}\,\mathrm{W\,cm^{-2}}$ and at a low-laser field of $eF_\ell=-2\,\mathrm{eV\,Å^{-1}}$, we failed to achieve a proper fit of the simulated $P(\epsilon)$ data by the thermal distribution, Eq. (7), with $\epsilon_{av}=0.37\,\mathrm{keV}$ being obtained from the first moment of the simulated energy distribution. As is apparent from Fig. 14, at this lower laser field the fit of simulated $P(\epsilon)$ to $P_T(\epsilon)$ ($\epsilon_{av}=0.37\,\mathrm{keV}$) reveals marked deviations (Fig. 14), implying that a self consistent fit for the simulated $P(\epsilon)$ data by a thermal distribution is inapplicable. The latter high-intensity low-field result is surprising, and may be due to the spatial ''shrinking'' of the nanoplasma electron cloud (Fig. 11). The average energies $\epsilon_{av}=54.1\,\mathrm{eV}$ at $I=10^{16}\,\mathrm{W\,cm^{-2}}$ and $\epsilon_{av}=0.56–0.37\,\mathrm{keV}$ at $I=10^{18}\,\mathrm{W\,cm^{-2}}$, obtained from the first moment of the simulated $P(\epsilon)$ distributions, are close (within a numerical factor of ~ 2) to the ϵ_{av} versus r/R energy spatial distribution data obtained inside the cluster, where the electron density is high (Figs. 11 and 12).

V. CONCLUDING REMARKS

Interesting features of extreme cluster multielectron ionization in ultraintense laser fields pertain to electron dynamics and to the characteristics of the nanoplasma in large finite systems. Ultrafast femtosecond electron dynamics, which were explored herein for a laser-cluster coupled system, constitutes a research area. Ultrafast cluster dynamics is not limited to the dynamics of ions on the time scale of nuclear motion, but is extended to the realm of electron dynamics.[28] Examples for electron dynamics, which come to mind, pertain to condensed phase and surface electron–electron collisions and plasmon dynamics, electron-metal surface[29] and cluster[30] image state dynamics, incipient electron localization in liquid helium,[31] electron-hole coherence of Wannier excitons and exciton wave-packet dynamics in semiconductor clusters and quantum dots,[28] electron tunneling from internal bubble states in large $(\mathrm{He})_n$ ($n>10^{14}$) clusters,[32] and electron tunneling from a nanotip in real time.[33] Electron dynamics involves changes in electronic states, without the involvement of nuclear motion, bypassing the constraints imposed by the Franck–Condon principle. Franck–Condon constraints are ubiquitous in a variety of chemical and physical ultrafast processes, e.g., electron transfer,[34] energy transfer,[35] and transition-state time-resolved spectroscopy.[36] Electron dynamics on the femtosecond (and attosecond) time scale provides phenomena in condensed phase, surface, and cluster dynamics. The phenomena of inner ionization, nanoplasma dynamics, and outer ionization in clusters coupled to an ultraintense laser field, constitutes a new realm of electron dynamics on the time scale of a few to tens of femtoseconds.

The present study of electron dynamics pertains to a coupled cluster-laser system. From our simulations and analyses it is apparent that electron dynamics is driven by the light pulse of the ultraintense laser. Accordingly, the time scales for electron dynamics are expected to be affected by the laser pulse shape. Two types of time scales for electron dynamics should be considered in this context. First, the ''absolute'' times interrogated by the time scale of the laser pulse, e.g., the attainment of the laser onset of the truncated Gaussian pulse at $t=t_s$, and the attainment of the laser peak at $t=0$ for the Gaussian pulse, Eqs. (1) and (2) used herein. These ''absolute'' time scales provide information on the interrogation of the laser pulse by the cluster, and are of limited dynamic interest. Second, ''relative'' time scales for electron dynamics, e.g., the characteristic times τ_{ii} and τ_{oi} for inner/outer ionization, the time lag $\Delta\tau_{OI}$ between outer-inner ionization (Sec. III), and the times for the population rise, decay, and persistence of the nanoplasma (Sec. IV), provide significant dynamic information. In the present study a simple Gaussian laser pulse shape, Eqs. (1) and (2), was employed. It is expected that the laser pulse shape will affect both the ''relative'' and the ''absolute'' time scales for electron dynamics. In recent years impressive progress was made in the field of laser pulse shaping in the context of control of laser induced processes[37,38] The utilization of laser pulse shaping[37,38] to the experimental, computational, and theoretical studies of extreme cluster multielectron ionization, i.e., inner/outer ionization and nanoplasma dynamics, will be of considerable interest. Another interesting problem involves the experimental interrogation of cluster electron dynamics. This may be accomplished by pump–probe femtosecond experiments, which are similar, in principle, to those applied by Zweiback, Ditmire, and Peny for cluster nuclear dynamics,[39] providing information on the dynamics of the formation of the nanoplasma and of its decay.

Features of nonequilibrium electronic states of large finite systems emerge for the properties of the nanoplasma in molecular clusters. According to our analysis, the nanoplasma has the following features:

(a) Nanoplasma electrons are confined to the cluster or to its vicinity.

(b) The nanoplasma is positively charged.

(c) The nanoplasma electron density is high. The electron density can be inferred from the maximal number of nanoplasma electrons n_p in the persistent nanoplasma (at $I=10^{16}\,\mathrm{W\,cm^{-2}}$) or in the transient nanoplasma (at $I=10^{18}\,\mathrm{W\,cm^{-2}}$). For Xe_n clusters (Figs. 2 and 3) $n_p=3$ for the persistent nanoplasma ($t>50\,\mathrm{fs}$), while $n_p\simeq 4$ for the transient nanoplasma. The maximal number, $n_p\simeq 3-4$, of electrons per Xe atom localized within the cluster can be used to estimate the average electron density $\rho_P=n_p/(4\pi/3)R_{\mathrm{Xe}}^3$, where $R_{\mathrm{Xe}}=3.3\,\mathrm{Å}$ is the radius of a Xe atom. The average electron density in the persistent or the transient nanoplasma is $\rho_P\simeq(2-3)10^{22}\,\mathrm{cm^{-3}}$. This high-electron density is comparable to that of a metal.

(d) Nanoplasma high energies. High average electron energies are exhibited within the nanoplasma, with ϵ_{av} manifesting a marked laser peak intensity dependence ($\epsilon_{av}\propto I^{1/2}\propto F_M$). The average energies for nanoplasma electrons in Xe_{1061} clusters at $I=10^{16}\,\mathrm{W\,cm^{-2}}$ is $\epsilon_{av}=54\,\mathrm{eV}$, while at $I=10^{18}\,\mathrm{W\,cm^{-2}}$ the average energy increases to $\epsilon_{av}=0.4–0.6\,\mathrm{keV}$. Beyond the cluster boundary ($r>R$) the average electron energy markedly increases, reaching electron energies for outer ionization of Xe_n clusters in the range of ~ 1.2 keV ($n=249$ at $I=10^{16}\,\mathrm{W\,cm^{-2}}$) to ~ 40 keV ($n=2172$ at $I=10^{18}\,\mathrm{W\,cm^{-2}}$).

(e) Nanoplasma spatial inhomogeneity. The nanoplasma is spatially inhomogeneous, with the (laser field induced) extension of the electron cloud beyond the cluster boundary at $I = 10^{16}$–10^{18} W cm^{-2} and, conversely, the effect of spatial shrinking of the electron cloud within the cluster at a very high intensity ($I = 10^{18}$ W cm^{-2}).

(f) Nanoplasma angular anisotropy. A marked bias of the electron angular distribution in the direction of the laser field is exhibited. This angular bias is manifested for the exterior electron at high laser fields for $I = 10^{16}$ W cm^{-2} and for the entire electron cloud at $I = 10^{18}$ W cm^{-2}.

(g) Nonuniform angular distribution of the electron velocities. The velocity distribution within the nanoplasma is not uniform, indicating nonrandomness of the velocities.

(h) Deviations of the electron energy distribution within the nanoplasma from a thermal distribution. For high laser fields over the entire intensity domain $I = 10^{16}$–10^{18} W cm^{-2} studied herein, the energy distribution in the nanoplasma is close to thermal. The persistent long-lived nanoplasma produced at $I = 10^{16}$ W cm^{-2} can be reasonably well described by a thermal distribution, while marked deviations from thermal distribution were recorded for a low laser field at $I = 10^{18}$ W cm^{-2}. It is an open question whether the thermal distribution, Eq. (7), is appropriate for the description of the thermal equilibrium in the nanoplasma.

(i) Response of the nanoplasma to an ultraintense laser field. This involves the quasiresonance mechanisms for the laser-nanoplasma interaction, which leads to cluster outer ionization.

A major open question in the context of the response of the nanoplasma pertains to the description of the optical properties of the nanoplasma in an ultraintense laser field. We have seen that the electron density in the nanoplasma $[\rho_P \sim (2-3)10^{22}\,\mathrm{cm}^{-3}]$ is similar to that of a metal. One should inquire whether and how one can define collective plasma oscillations in the finite nanoplasma. A heuristic approach will involve the use of the electron density ρ_P to characterize the plasma frequency[40] $\omega_p = (4\pi e^2 \rho_P / 3 m_e)^{1/2}$ (where the numerical factor of 1/3 originates from the response of a spherical finite cluster whose radius is considerably smaller than the wavelength of light). The plasma frequency $\omega_p = (5-7)10^{15}\,\mathrm{s}^{-1}$ corresponds to energies of $\hbar\omega_p \simeq 4-5$ eV, which exceeds by a numerical factor of ~ 3 the photon energy (1.44 eV) of the ultrafast laser employed in the present simulations. Further exploration of the nanoplasma response will be of interest in the context of the optical properties of the nanoplasma in the Coulomb exploding cluster, which can be interrogated, in principle, by time-resolved femtosecond spectroscopy.

ACKNOWLEDGMENT

This research was supported in part by the Binational German-Israeli Program on Laser-Matter Interaction.

[1] T. Ditmire, T. Donnelly, A. M. Rubenchik, R. W. Falcone, and M. D. Perry, Phys. Rev. A **53**, 3379 (1996).
[2] T. Ditmire, J. W. G. Tisch, E. Springate, M. B. Mason, N. Hay, R. A. Smith, J. Marangos, and M. H. R. Hutchinson, Nature (London) **386**, 54 (1997).
[3] T. Ditmire, E. Springate, J. W. G. Tisch, Y. L. Shao, M. B. Mason, N. Hay, J. P. Marangos, and M. H. R. Hutchinson, Phys. Rev. A **57**, 369 (1998).
[4] J. V. Ford, O. Zhong, L. Poth, and A. W. Castleman, Jr., J. Chem. Phys. **110**, 6257 (1999).
[5] M. Lezius, V. Blanchet, D. M. Rayner, D. M. Villeneuve, A. Stolov, and M. Yu. Ivanov, Phys. Rev. Lett. **86**, 51 (2001).
[6] E. Springate, N. Hay, J. W. G. Tisch, M. B. Mason, T. Ditmire, M. H. R. Hutchinson, and J. P. Marangos, Phys. Rev. A **61**, 063201 (2000).
[7] J. Zweiback, R. A. Smith, T. E. Cowan, G. Hays, K. B. Wharton, V. P. Yanovsky, and T. Ditmire, Phys. Rev. Lett. **84**, 2634 (2000).
[8] S. Teuber, T. Töppner, T. Fennel, J. Tiggesbäumker, and K. H. Meiwes-Broer, Eur. Phys. J. D **16**, 59 (2001).
[9] D. A. Card, E. S. Wisniewski, D. E. Folmer, and A. W. Castleman, Jr., J. Chem. Phys. **116**, 3554 (2002).
[10] T. Ditmire, Phys. Rev. A **57**, R4094 (1998).
[11] I. Last and J. Jortner, Phys. Rev. A **60**, 2215 (1999).
[12] K. Ishikava and T. Blenski, Phys. Rev. A **62**, 063204 (2000).
[13] I. Last and J. Jortner, Phys. Rev. A **62**, 013201 (2000).
[14] I. Last and J. Jortner, Phys. Rev. Lett. **87**, 033401 (2001).
[15] I. Last and J. Jortner, Phys. Rev. A **64**, 063201 (2001).
[16] V. P. Krainov and A. S. Roshchupkin, Phys. Rev. A **64**, 063204 (2001).
[17] V. P. Krainov and M. B. Smirnov, Phys. Rep. **370**, 237 (2002).
[18] I. Last and J. Jortner, J. Phys. Chem. A **106**, 10877 (2002).
[19] Ch. Sudschlag and J. M. Rose, Phys. Rev. Lett. **89**, 173401 (2002).
[20] Ch. Sudschlag and J. M. Rose, Phys. Rev. A **67**, 013404 (2003).
[21] T. Zuo and A. D. Bandrauk, Phys. Rev. A **52**, R2511 (1995).
[22] T. Seideman, M. Yu. Ivanov, and P. B. Corkum, Phys. Rev. Lett. **75**, 2819 (1995).
[23] I. Last and J. Jortner, Phys. Rev. A **58**, 3826 (1998).
[24] S. Augst, D. Strickland, D. D. Meyerhofer, S. L. Chin, and J. Eberly, Phys. Rev. Lett. **63**, 2212 (1989).
[25] I. Last and J. Jortner, J. Chem. Phys. **120**, 1336 (2004), preceding paper.
[26] J. Liu, R. Li, P. Zhu, Z. Xu, and J. Liu, Phys. Rev. A **64**, 033426 (2001).
[27] I. Last and J. Jortner (unpublished).
[28] J. Jortner, Proc. R. Soc. London, Ser. A **356**, 477 (1998).
[29] T. Hertel, F. Konesel, H. Wolf, and G. Ertel, Phys. Rev. Lett. **76**, 535 (1996).
[30] M. Rosenblit and J. Jortner, J. Phys. C **98**, 9365 (1994).
[31] M. Rosenblit and J. Jortner, Phys. Rev. Lett. **75**, 4079 (1995).
[32] M. Rosenblit and J. Jortner (unpublished).
[33] D. Botkin, J. Glass, D. Chemla, D. G. Ogletree, H. Salmeron, and S. Weiss, Appl. Phys. Lett. **69**, 1321 (1996).
[34] M. Bixon and J. Jortner, Adv. Chem. Phys. **106**, 35 (1999).
[35] T. Forster, Ann. Phys. (Leipzig) **6**, 55 (1948).
[36] M. Hartman, A. Heidenreich, J. Pittner, V. Bonacic-Koutecky, and J. Jortner, J. Chem. Phys. **108**, 3096 (1998).
[37] H. Rabitz, R. De Vivie-Riedler, M. Motakus, and K. Kompa, Science **288**, 824 (2000).
[38] T. Brixner, M. H. Domraus, P. Niklaus, and R. G. Gerber, Nature (London) **414**, 57 (2001).
[39] J. Zweiback, T. Ditmire, and M. D. Peny, Phys. Rev. A **59**, R3166 (1999).
[40] R. Kubo and T. Nugamiya, *Solid State Physics* (McGraw-Hill, New York, 1969), pp. 112–119.